ADVANCED FUNCTIONAL MATERIALS
www.afm-journal.de

www.MaterialsViews.com

Hierarchical Carbon–Nitrogen Architectures with Both Mesopores and Macrochannels as Excellent Cathodes for Rechargeable Li–O_2 Batteries

*Zhang Zhang, Jie Bao, Chen He, Yanan Chen, Jinping Wei, and Zhen Zhou**

Lithium–oxygen batteries are attracting more and more interest; however, their poor rechargeability and low efficiency remain critical barriers to practical applications. Herein, hierarchical carbon–nitrogen architectures with both macrochannels and mesopores are prepared through an economical and environmentally benign sol–gel route, showing high electrocatalytic activity and stable cyclability over 160 cycles as cathodes for Li–O_2 batteries. Such good performance owes to the coexistence of macrochannels and mesopores in C–N hierarchical architectures, which greatly facilitate the Li^+ diffusion and electrolyte immersion, as well as provide an effective space for O_2 diffusion and O_2/Li_2O_2 conversion. Additionally, the mechanism of oxygen reduction reactions is discussed with the N-rich carbon materials through first-principles computations. The lithiated pyridinic N provides excellent O_2 adsorption and activation sites, and thus catalyzes the electrode processes. Therefore, hierarchical carbon–nitrogen architectures with both macrochannels and mesopores are promising cathodes for Li–O_2 batteries.

1. Introduction

Rechargeable Li–O_2 batteries have been attracting much attention due to their extremely high theoretical energy density, and hold promise to meet the energy target for batteries in automotive applications.[1–3] A typical Li–O_2 battery is composed of a metallic lithium anode, non-aqueous electrolyte and a porous air cathode. Among these components, the air cathode becomes the bottleneck in Li–O_2 batteries, and better performances can be obtained by accelerating the reaction kinetics with the development of advanced air cathodes. Upon discharge, O_2 reacts with Li^+ to form insoluble and insulating discharge product (Li_2O_2), and these discharge products stored in the air cathode can block the electrolyte and oxygen pathways, leading to poor electrochemical performances of Li–O_2 batteries.[4] Advances in nanostructured air cathode design and preparation are urgent to fully harvest high energy density of Li–O_2 batteries. Recently, it has been reported that an air cathode composed of abundant hierarchical mesopores and macropores tends to improve the electrochemical performances significantly. Mesopores can effectively improve the electrolyte immersion, and provide more active sites for electrochemical reactions, while macropores can provide large space to avoid the blockage of electrolyte and oxygen pathways, which are very critical for O_2 diffusion and reversible conversion.[5] Therefore, the development of novel carbon cathodes with desired porosity and large specific surface area becomes the focus of this field.[6–8]

Many efforts have been made to design materials with unique morphology and porous structure. Previously, different kinds of carbon materials were prepared for air cathodes, including mesocellular carbon foams,[6] carbon nanofibers,[7] and mixed carbon materials.[9] Besides, graphene and carbon nanotubes with various morphologies improved the electrochemical performance of Li–O_2 batteries significantly.[10–13] In addition to various porous structures, the surface chemistry of carbon materials also performs important functions in Li–O_2 batteries. Both computations and detailed experiments have proved that doping foreign atoms is an effective way to achieve better performances. Recent studies have disclosed that nitrogen-doped carbon cathodes showed enhanced performances, especially nitrogen-doped graphene manifested higher electrocatalytic activity than pristine graphene towards oxygen reduction reactions (ORR) in nonaqueous electrolytes.[14–16] These nitrogen-doped carbon materials have ever been extensively applied to ORR in aqueous electrolytes for fuel cells.[17,18] Due to the lone electron pairs of nitrogen atoms, which can connect with the sp^2-hybridized carbon frame to form a delocalized conjugated system,[19,20] great improvement could be achieved with enhanced reactivity and electrocatalytic activity. Although the improvement could be obtained by modifying the surface of carbon materials with low N contents, the efforts involving N-rich carbon materials have not been made to Li–O_2 batteries.

In this work, we prepared hierarchical macrochannel/mesopore carbon-nitrogen (HMCN) architectures through a

Z. Zhang, J. Bao, C. He, Y. Chen, Prof. J. Wei, Prof. Z. Zhou
Tianjin Key Laboratory of Metal and Molecule Based Material Chemistry
Key Laboratory of Advanced Energy Materials Chemistry (Ministry of Education)
Computational Centre for Molecular Science
Institute of New Energy Material Chemistry
Collaborative Innovation Center of Chemical Science and Engineering (Tianjin)
Nankai University
Tianjin 300071, P. R. China
E-mail: zhouzhen@nankai.edu.cn

DOI: 10.1002/adfm.201401581

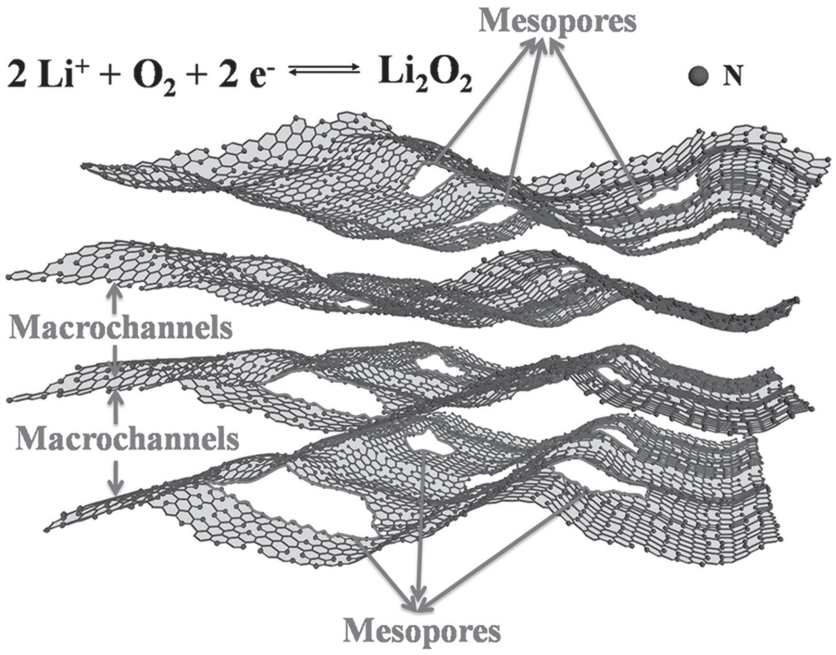

Figure 1. Schematic illustration of hierarchical carbon-nitrogen material with both macrochannels and mesopores as cathodes for Li–O_2 batteries.

facile and economical sol–gel route. The ordered mesopores in HMCN can efficiently store discharged products and facilitate Li^+ diffusion and electron transfer (**Figure 1**). More importantly, macrochannels, which exist among nanosized slices, provide necessary space for O_2 and electrolyte diffusion (Figure 1). Interestingly, HMCN contains high-level pyridinic N, which plays an important role of improving ORR activity. The C–N hierarchical architecture delivered higher electrochemical activity and more stable cyclability over 160 cycles as air cathodes for Li–O_2 batteries. To illustrate the excellent electrocatalytic effect of HMCN, we also conducted first-principles computations and found that pyridinic N catalyzes electrochemical processes by affiliating and activating O_2 after lithiation. This finding provided valuable clues to materials design for cathodes of Li–O_2 batteries.

2. Results and Discussion

Figure 2a,b clearly shows the scanning electron microscope (SEM) images of HMCN architectures with interesting morphology. The HMCN architecture consists of many nanoslices. Macrochannels with ≈150 nm in height form among the piled nanoslices. This favorable porous character could connect with each other and act as oxygen transport channels to facilitate oxygen diffusion and accommodate discharged products during the electrochemical process.[21] The detailed structure of HMCN was further confirmed by transmission electron microscope (TEM) images (Figure 2c,d). The big board contains lots of nanosheets and particles, and pores of different sizes are homogenously distributed within the small nanosheets. The high-magnification TEM image (Figure 2e,f) clearly presents typical pores with different shapes. The pores with different morphologies formed during the calcination procedure. The composite was further characterized by N_2 adsorption-desorption experiments (**Figure 3**a); the specific surface area of HMCN reaches 254.8 m^2/g and a typical mesoporous structure with type-IV isotherm can be deduced. The pore size distribution can be observed in Figure 3b, and the dominant pore size of 3–5 nm demonstrates the typical mesoporous structure. In a typical synthesis process, citric acid was utilized as the carbon source and mixed well with massive urea to form a sol and then a gel, and the formation of pores may be caused by the release of gases (CO_2, H_2O, and NH_3) after calcinating the gel.

Actually, HMCN also contained rich N elements decomposed from urea when calcinating the gel. X-ray photoelectron spectroscopy (XPS) confirms the state of nitrogen and carbon in HMCN. The peaks at 284.8, 285.9, 288.9, and 291.4 eV were assigned to sp^2 C-sp^2 C, N-sp^2 C, N-sp^3 C bonds and C = O in high-resolution C1s spectra (Figure 3c). The high-resolution N1s peaks demonstrate three types of N (pyridinic-N, pyrrolic-N, and oxidized-N) (Figure 3d), and these N states have also been found in previous reports.[22,23] The content of pyridinic-N (42%) is

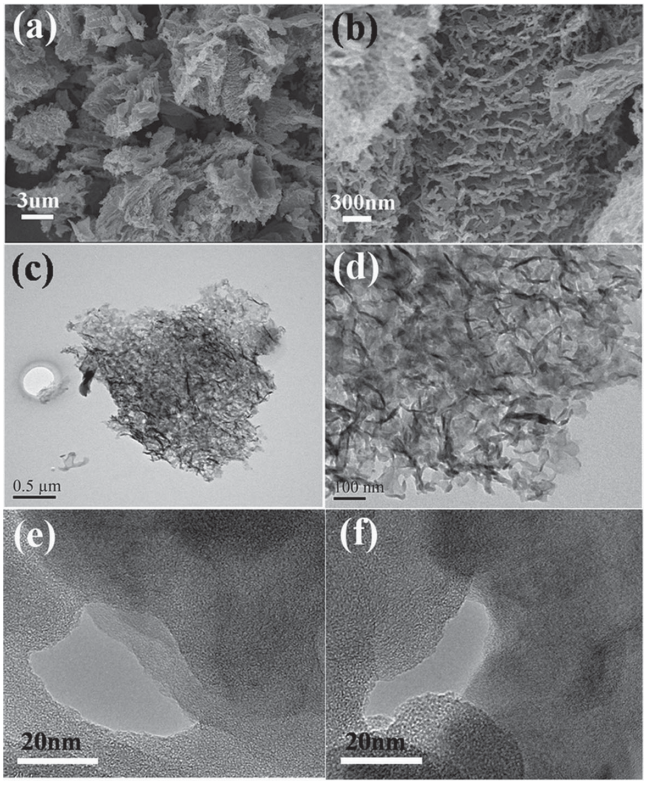

Figure 2. a,b) SEM images with different magnifications of HMCN. c,d) TEM images with different magnifications of HMCN. e,f) present the pores in HMCN.

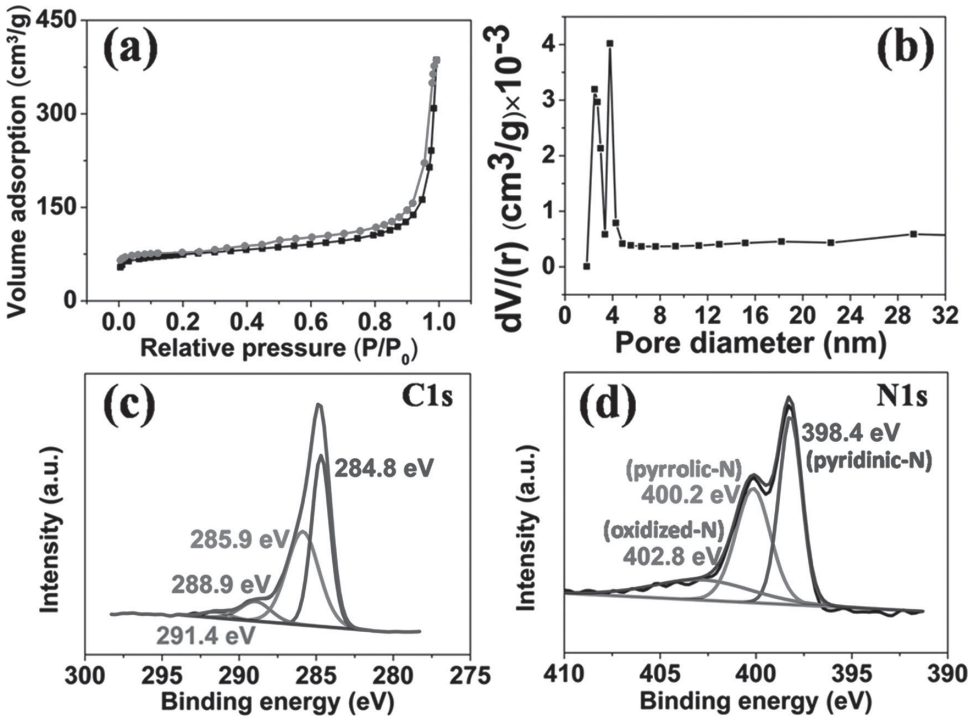

Figure 3. a) N_2 adsorption-desorption isotherms of HMCN. b) The pore-size distribution of HMCN. c) C1s, and d) N1s XPS of HMCN.

the highest among all three types of N through the calculation of the N1s spectra. Actually, N could be regarded as an n-type dopant for carbon materials, which assists in the formation of disordered carbon nanostructure and facilitates the ORR process,[20] and especially pyridinic N plays a significant role of ORR activity.[24,25] Electron energy loss spectroscopy (EELS) was also conducted to further confirm the state of C and N. Figure S1 (Supporting Information) shows a typical spectrum with two visible edges starting at 282 eV and 398 eV, corresponding to the characteristic K-shell ionization energy of C and N.[26,27] The two bands corresponding to C and N can be well assigned to the 1s-π^* antibonding orbital, followed by another band attributed to the 1s-σ^* antibonding orbital. This type of EELS edge structure proves that C and N are sp^2 hybridized.[27] Obviously, the representative EELS of HMCN shows more apparent peaks of N than those of nitrogen-doped graphene,[23] which may be caused by its higher content in HMCN after calcination. As shown in the energy dispersive X-ray spectroscopy (EDX) (Figure S2a–c, Supporting Information), C and N are uniformly distributed in HMCN. Elemental analysis quantitatively confirmed the content of C and N, and the amount of N is up to 28.1 wt% (Figure S2d, Supporting Information).

The composite was also characterized by Raman spectroscopy (Figure S2e, Supporting Information), in which the "D" band appears at ≈1348 cm^{-1} and the "G" band at ≈1584 cm^{-1}. The ratio of the intensities of these two bands (I_D/I_G) is 1.16, which is an important indicator of the carbon crystallization.[28] The higher I_D/I_G ratio of HMCN also implies more defects in graphite-like layers, which is caused by the introduction of more nitrogen atoms.[29]

HMCN presents many outstanding structural and compositional characters, and demonstrates possible applications to Li–O_2 batteries. The discharge and charge measurements were performed in the voltage range of 2.0–4.3 V for HMCN cathodes. Note that we also tested the pristine carbon paper for comparison, and it showed low electrochemical activity at different current densities of 50 mA/g and 100 mA/g (Figure S3, Supporting Information). Both the applied current (mA/g) and achieved capacity (mAh/g) were normalized to the weight of HMCN. As shown in **Figure 4**a, the HMCN cathode provided a discharge capacity of ≈3200 mAh/g at the current density of 50 mA/g, and a high average operating voltage of 2.75 V, which was consistent with N-doped carbon materials in previous reports.[14,16] Even compared with binder-free nitrogen-doped carbon nanotubes, the HMCN cathode presented better discharge capacity and more stable platform.[30] The HMCN cathode maintained high capacity (≈3000 mAh/g) and stable discharge platform (2.62 V) at the current density of 100 mA/g. The HMCN cathodes also showed lower overpotentials than other carbon materials or N-doped carbon materials during the cycle tests.[7,12,29,31,32] In the first cycle (Figure 4b), the HMCN cathode exhibits stable charge and discharge platforms, and a relatively low charge plateau at 4.0 V; even in the 100th cycle, the charge–discharge platforms were still almost consistent with those of the 1st cycle. In contrast, the ketjen black (KB) cathode showed high overpotential and unstable platform only after 24 cycles (Figure S4, Supporting Information). Compared with various carbon materials or heteroatom-doped carbon materials in previous reports,[5,11,16,33] the HMCN cathode also showed low overpotential and stable charge–discharge platform after long cycles. The superior performance of the HMCN cathode is probably attributed to the hierarchical structure of both mesopores and macrochannels, which provide optimized oxygen transport network.[16]

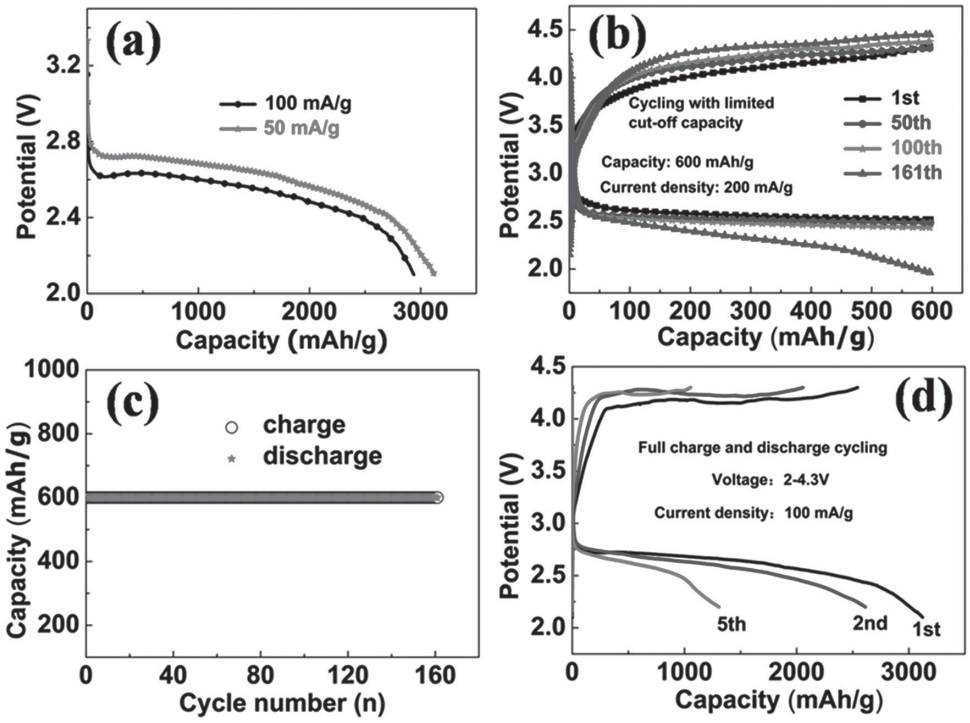

Figure 4. a) The discharge profiles of the HMCN cathode at various current densities of 50 and 100 mA/g. b) The limited depth of discharge at 600 mAh/g at a current of 200 mA/g with the HMCN cathode. c) The corresponding plot of discharge and charge capacity against cycle number, and d) full discharge/charge curves between 2.0–4.3 V at 100 mA/g.

As discussed above, nitrogen-doped carbon materials showed unsatisfactory cyclability as air cathodes in Li–O_2 batteries in previous reports; even the binder-free nitrogen-doped carbon nanotubes showed only 9 cycles with a restriction in the capacity of 500 mAh/g at the current density of 0.05 mA cm^{-2} (75 mA/g).[30] Therefore, the improvement in cyclability is essential for the wide applications of Li–O_2 batteries in the future. In order to avoid the over-growth of discharged products induced by deep discharge, we tested the batteries with a cut-off capacity of 600 mAh/g at a current density of 200 mA/g. The batteries showed excellent cyclability over 160 cycles in the atmosphere of O_2, with stable charge and discharge platform (Figure 4b). The cells with HMCN cathodes exhibited excellent cyclability over 160 cycles (Figure 4c), much longer than those (24 cycles) of universal KB cathodes (Figure S4, Supporting Information). Moreover, HMCN cathodes also presented more stable platform and lower overpotential than KB. Even compared with other precious catalysts including Mn-Ru binary oxides,[34] and carbon nanotube@RuO_2 composites,[35] the HMCN composite showed better cyclablity. Very recently, Dai and coworkers have reported that vertically aligned N-doped coral-like carbon fiber arrays also showed excellent cyclability and significantly low overpotential,[36] manifesting the prospect of N-doped carbon materials to improve the electrochemical performance of Li–O_2 batteries. The cycling performance of HMCN was also tested in the full discharge/charge cycle protocols between 2.0 and 4.3 V (Figure 4d). Although the stable charge/discharge platform was preserved, the capacity decay became obvious after the fifth cycle, which was consistent with the results of nitrogen-doped carbon nanotubes obtained in Li-air batteries.[29] Actually, stable full discharge/charge cyclability is typically hard to realize due to the accumulation of the discharge product and instability of the electrolyte.[37–39] This problem could be solved to some degree by introducing noble metals[40] and stable binders.[41–43] As show in Figure S5 (Supporting Information), a Nafion binder improved the initial capacity of the HMCN cathode; however, the cyclablity was not enhanced, and many efforts are still necessary for the realization of full discharge/charge cyclability.

To further explore the insight of discharge and charge processes of Li–O_2 batteries with HMCN cathodes, the morphologies of discharged and charged cathodes were observed through SEM. The characterizations of charge–discharge processes were all limited to the cut-off capacity of 600 mAh/g at the current density of 200 mAh/g. After the 10th discharge (**Figure 5**a), the insoluble species precipitated on the surface of HMCN, and toroidal Li_2O_2 was also observed with the typical morphology in previous reports.[44,45] After the 10th charge, the porous structure was mostly recovered in the HMCN cathode (Figure 5b). The ex-situ Raman spectroscopy (Figure 5c) suggests that the peak of Li_2O_2 is not observed due to its low content probably, yet it is obvious that the I_D/I_G ratio of HMCN is much higher in the 10th charge than in the 10th discharge, which indirectly confirms that N-induced defects in graphite-like layers recovered after the charging process, and the discharged products can be efficiently decomposed during the charging process. In order to accurately characterize the discharged products during the 10th cycle, Fourier-transform infrared (FTIR) spectroscopy was conducted to identify the discharge products of HMCN. As shown in Figure 5d, the characteristic peak of Li_2O_2 is observed

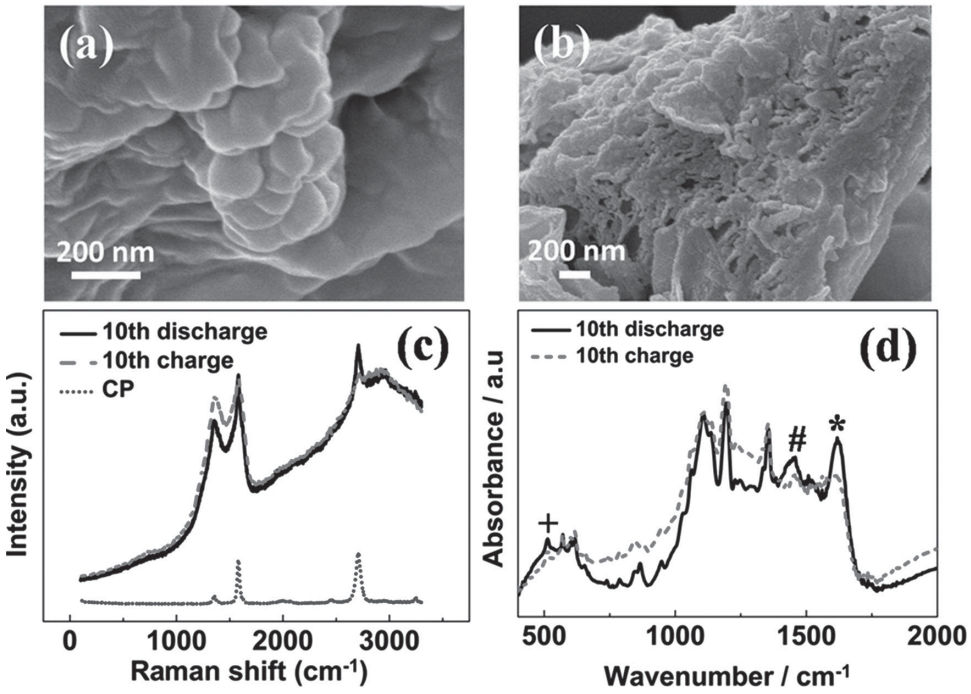

Figure 5. SEM images of HMCN cathode a) in the 10th discharge and b) in the 10th charge. c) Raman and d) FTIR spectra of the HMCN cathode in the 10th discharge and charge process. The signals of Li_2O_2, HCO_2Li, and CH_3CO_2Li are marked as +, #, *, respectively.

at 518 cm^{-1}. In addition to the peaks arising from Li_2O_2, the peaks around 1450 cm^{-1} and 1620 cm^{-1} could be assigned to HCO_2Li and CH_3CO_2Li, which were reported commonly with ether-based electrolytes when carbon materials were used as air cathodes.[38,45,46] By comparing the 10th discharge and charge process, we found that the peak intensity of HCO_2Li and CH_3CO_2Li apparently decreased after the charge process, which was consistent with the Raman characterization. Besides FTIR, the XRD patterns of the cathode during the first cycle are also shown in Figure S6 (Supporting Information). Li_2CO_3, CH_3CO_2Li and Li_2O_2 can be clearly observed during the 1st discharge process, after the subsequent charge process, the peaks of Li_2CO_3, CH_3CO_2Li, and Li_2O_2 disappear obviously. In addition, the XRD curve becomes flat and smooth after the charge process, indicating the decomposition of discharge products. These results verify the superior activity of HMCN in electrocatalyzing the discharge products and improving the electrochemical cyclic stability during discharge-charge processes.

To throw light on the mechanism of ORR on N-rich carbon sheets, we performed preliminary first-principles computations on the electrochemical processes. Since adsorption occurs between two phases (solution and HMCN), we hypothesized that it is the strong adherence to Li^+ and O_2 that contributes to HMCN's catalysis. Therefore, the adsorption energies of Li^+ and O_2 on HMCN were computed and the results are summarized in **Table 1**.

It is interesting to see that only the carbon sheet with pyridinic N is thermodynamically favorable to attract Li^+. This provides convincing evidence that pyridinic N introduces the affiliation of Li^+ into carbon sheet. By comparing all adsorption energies, we found that the first reaction process is the adsorption of Li^+ on pyridinic N. Since pyridinic carbon sheet attracts Li^+ exclusively, PyriCS represents pyridinic carbon sheet in the second column. Besides, in the second column we find that Li atom has the strongest attraction to O_2, and LiPyriCS (short for lithiated PyriCS) ranks the next. In solution conditions isolated Li atoms could not exist experimentally; therefore, O_2 tends to attach to LiPyriCS. Such assertion indicates that before O_2 is adhered to HMCN, $LiPyriCS^+$(short for Li^+-adsorbing PyriCS) is already reduced to neutral state. According to the charge difference analysis (Figure S7, Supporting Information), when an electron is added to the system (electrochemical reduction), the added electron is dispersed on the carbon sheet, which means that Li remains ionic in the center, and cannot be reduced to metallic Li. Therefore, the mechanism is that Li^+ compensates the electron dispersed on the carbon sheet, and it is the electron-redundant carbon sheet that has stronger interaction with O_2. Additionally, graphene and its

Table 1. Computed adsorption energies (eV) of Li^+ and O_2. In the first row, Li^+ adsorption energies were considered for graphene, pyridinic N, pyrrollic N and the edge. Based on the results in the first row, the O_2 adsorption at lithiated pyridinic N was taken into account and named by LiPyriCS.

	Graphene	Pyridinic	Pyrrollic	Edge	LiPyriCS	$LiPyriCS^+$	Li^+	Li
Li^+ Adsorption	0.752	–2.559	0.166	1.231	–	–	–	–
O_2 Adsorption	–0.096	–0.099	0.297	–0.138	–0.411	4.982	3.340	–1.064

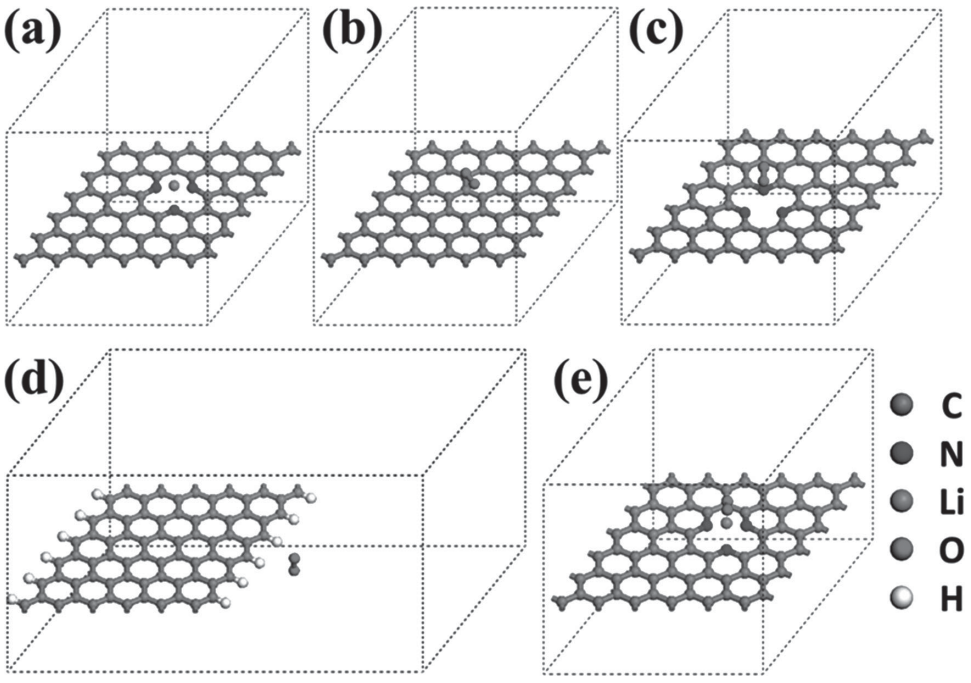

Figure 6. Scheme of all thermodynamically stable structures for Li or/and O_2 adsorption. Periodicity is shown here with vacuum layers of 20 Å. Note that, to model the interaction of the graphene edge with O_2 or Li^+ (not shown here) we build a ribbon and enlarge one leg of the lattice. a) Li^+ lies at the center of three N atoms. b–e) Adherence of O_2 on graphene (parallel), pyridinic graphene (parallel), edge (vertical) and lithiated pyridinic graphene (leaned), respectively.

edges are O_2-affiliating according to our results, which mean that they will help catch O_2 onto HMCN. The stable configurations are shown in **Figure 6**. We investigated the bond length of adsorbed O_2 at possible sites, and the results are shown in Table S1 (Supporting Information). All the considered adsorption sites are capable to elongate the O–O bond and activate O_2. The O_2 adsorbed on LiPyriCS exhibits the longest bond length (1.269 Å), suggesting that LiPyriCS site is the most capable to activate O_2. Considering that the pyridinic N and graphene sites are dominant in HMCN, it is reasonable that PyriCS, which gives birth to LiPyriCS, has the most advantage to catalyze the formation of discharge product.

Based on above discussion, we put forward the following three reactions as the crucial processes in HMCN cathodes:

$$Li^+ + PyriCS \rightarrow LiPyriCS^+ \quad (1)$$

$$LiPyriCS^+ + e^- \rightarrow LiPyriCS \quad (2)$$

$$LiPyriCS + O_2 \rightarrow LiPyriCSO_2 \quad (3)$$

Herein the reactions are Li^+ adsorption, electron transfer and O_2 adsorption, respectively. In order to put these reactions into practice, we interpreted that before discharging process happens, Li^+ is already adhered on the pyridinic carbon sheets. The adsorbed Li^+ balances the negative charge (one more electron) on PyriCS. LiPyriCS has the strongest interaction with O_2, providing adsorption sites for O_2. O_2 on LiPyriCS exhibits significant bond elongation, proving the catalytic effect of LiPyriCS. This explains why introducing pyridinic N, rather than other configurations, would effectively electrocatalyze the processes in our experiments. However, the electrochemical reactions of Li–O_2 batteries are extremely complicated, and much more investigations, from both computational and experimental sides, are needed to clarify the role of HMCN thoroughly.

3. Conclusion

In summary, mesoporous hierarchical carbon-nitrogen architectures were synthesized through a facile and convenient sol–gel method, and the so-prepared carbon material has a high content of nitrogen with homogeneous distribution. The C-N architectures were employed as air cathodes for Li–O_2 batteries and delivered high capacity and stable cyclability. The excellent performance was attributed to the hierarchical pore structures (ordered mesopores and macrochannels) and the introduction of nitrogen atoms, facilitating the kinetics in the electrochemical reactions. First-principles computations disclosed that pyridinic N can attach Li^+ and an electron to form LiPyriCS, which is a strong O_2 adsorption and activation site, and thus catalyzes electrochemical reactions. Therefore, HMCN could be a promising cathode material for the Li–O_2 batteries. This finding provides a new outlook for application of carbon materials to Li–O_2 batteries.

4. Experimental and Computational Section

Material Preparation: All the reagents were analytical grade without further purification. In a typical preparation process, 1.0 g citric acid

and 10 g urea were dissolved in 50 mL distilled water and 150 mL ethanol through magnetic agitation for 3 h to form a gel, and then the gel was dried at 100 °C overnight. The HMCN composite was obtained by calcining the gel for 4 h at 350 °C and then 650 °C for 10 h in Ar atmosphere. The same procedure has been applied to prepare Co–C or Ni–C material with the addition of Co or Ni salt.[47–49]

Material Characterization: XRD was performed on a D/MAX III diffractometer with Cu Kα radiation. Field emission SEM (FESEM) images were obtained on a JEOL-JSM7500 microscope. The EDX attached to the FESEM instrument was used to confirm the composition of the samples. TEM images were taken on FEITecnai G2F-20 equipped with EELS, and XPS was performed on Axis Ultra DLD (Kratos Analytical). N_2 adsorption/desorption isotherms were obtained by using ASAP 2020/Tristar 3000 Surface Area and Pore Size Analyzer. Raman spectra were conducted on a Renishaw inVia Raman spectrometer equipped with a 632.8 nm laser. FTIR spectroscopy was performed on NicoletMAGNA-560 FTIR spectrometer by using KBr pellets. Vario EL CUBE elemental analyzer was used to quantitatively confirm the contents of C and N.

Electrochemical Tests: The electrochemical behaviors were measured in swagelok cells with a 1.0 cm^2 hole placed on the cathode which enabled O_2 to flow in. The cells were assembled in a glove box filled with high-purity argon (O_2 and H_2O < 1 ppm). For the cathode preparation, slurry was obtained by mixing HMCN and polyvinylidenefluoride (PVDF) with the mass ratio of 9:1. The slurry was uniformly deposited on a circular piece of carbon paper, and then dried in an oven at 80 °C. Li foil was used as the anode, and polytetrafluoroethylene (PTFE) membrane as the separator. The electrolyte was 1 mol L^{-1} lithiumbis(trifluoromethanesulfonyl)imide (LiTFSI) dissolved in tetraethylene glycol dimethyl ether (TEGDME). The cells were discharged to 2 V on LAND-CT2001A testers for the first discharge. The cyclic tests were controlled with the cut-off capacity of 600 mAh/g at a current density of 200 mA/g, that is, the cells were discharged and charged for 3 h separately.

Computational Details: First-principles computations were performed within the framework of Vienna Ab-initio Simulation Package (VASP).[50,51] Density Functional Theory (DFT) with periodic boundary conditions was introduced to both geometry optimizations and static computations. Generalized gradient approximation (GGA) to the exchange-correlation functional by Perdew and Wang (PW91)[52] with spin polarization was applied, and projector augmented wave (PAW)[53] was used to describe the inner electrons of all atoms. Dispersion was employed to take weak interaction into account. A 3 × 3 × 1 k-point sampling in Brillouin zone and a cutoff energy of 400 eV were used to balance the computation expense and precision. According to our experiments, N is dispersed in the carbon sheet with different types. Pyridinic N, which is the most abundant, and pyrrolic N, which lies in the edges of the carbon sheet, were discussed. They were modeled in a two-dimensional (2D) monolayer and a one-dimensional (1D) nanoribbon, respectively. As a contrast, perfect graphene, representing the undoped region of the carbon sheet, was also investigated. Finally, to figure out the edge effect of the carbon sheet, a graphene ribbon with the edges saturated by hydrogen atoms was modeled to simulate the edge of the carbon sheet. Besides, O_2 and Li^+ were put into a $(11.8\ Å)^3$-cubic lattice to ensure a concentration of 1 mol L^{-1}.

Supporting Information

Supporting Information is available from the Wiley Online Library or from the author.

Acknowledgements

This work was supported by NSFC (21473094 and 21421001) and MOE Innovation Team (IRT13022) in China.

Received: May 15, 2014
Revised: July 8, 2014
Published online: September 1, 2014

[1] Y. Shao, F. Ding, J. Xiao, J. Zhang, W. Xu, S. Park, J. Zhang, Y. Wang, J. Liu, *Adv. Funct. Mater.* **2013**, *23*, 987.
[2] Y. C. Lu, B. M. Gallant, D. G. Kwabi, J. R. Harding, R. R. Mitchell, M. S. Whittingham, Y. Shao-Horn, *Energy. Environ. Sci.* **2013**, *6*, 750.
[3] J. Christensen, P. Albertus, R. S. Sanchez-Carrera, T. Lohmann, B. Kozinsky, R. Liedtke, J. Ahmed, A. Kojic, *J. Electrochem. Soc.* **2012**, *159*, R1.
[4] P. G. Bruce, S. A. Freunberger, L. J. Hardwick, J. M. Tarascon, *Nat. Mater.* **2012**, *11*, 19.
[5] Z. Guo, D. Zhou, X. Dong, Z. Qiu, Y. Wang, Y. Xia, *Adv. Mater.* **2013**, *25*, 5668.
[6] X. Y. Yang, P. He, Y. Y. Xia, *Electrochem. Commun.* **2009**, *11*, 1127.
[7] R. R. Mitchell, B. M. Gallant, C. V. Thompson, Y. Shao-Horn, *Energy Environ. Sci.* **2011**, *4*, 2952.
[8] J. Li, H. Zhang, Y. Zhang, M. Wang, F. Zhang, H. Nie, *Nanoscale* **2013**, *5*, 4647.
[9] Y. Zhang, H. Zhang, J. Li, M. Wang, H. Nie, F. Zhang, *J. Power Sources* **2013**, *240*, 390.
[10] G. Q. Zhang, J. P. Zheng, R. Liang, C. Zhang, B. Wang, M. Hendrickson, E. J. Plichta, *J. Electrochem. Soc.* **2010**, *157*, A953.
[11] H. D. Lim, K. Y. Park, H. Song, E. Y. Jang, H. Gwon, J. Kim, Y. H. Kim, M. D. Lima, R. Ovalle Robles, X. Lepro, R. H. Baughman, K. Kang, *Adv. Mater.* **2013**, *25*, 1348.
[12] Y. Li, J. Wang, X. Li, D. Geng, R. Li, X. Sun, *Chem. Commun.* **2011**, *47*, 9438.
[13] J. Xiao, D. Mei, X. Li, W. Xu, D. Wang, G. L. Graff, W. D. Bennett, Z. Nie, L. V. Saraf, I. A. Aksay, J. Liu, J. G. Zhang, *Nano Lett.* **2011**, *11*, 5071.
[14] P. Kichambare, J. Kumar, S. Rodrigues, B. Kumar, *J. Power Sources* **2011**, *196*, 3310.
[15] Y. L. Li, J. J. Wang, X. F. Li, D. S. Geng, M. N. Banis, R. Y. Li, X. L. Sun, *Electrochem. Commun.* **2012**, *18*, 12.
[16] H. Nie, H. Zhang, Y. Zhang, T. Liu, J. Li, Q. Lai, *Nanoscale* **2013**, *5*, 8484.
[17] L. Qu, Y. Liu, J. B. Baek, L. Dai, *ACS Nano* **2010**, *4*, 1321.
[18] Z. Xiang, D. Cao, L. Huang, J. Shui, M. Wang, L. Dai, *Adv. Mater.* **2014**, *26*, 3315.
[19] J. Zhang, X. Liu, R. Blume, A. Zhang, R. Schlogl, D. S. Su, *Science* **2008**, *322*, 73.
[20] K. Gong, F. Du, Z. Xia, M. Durstock, L. Dai, *Science* **2009**, *323*, 760.
[21] Z. L. Wang, D. Xu, J. J. Xu, L. L. Zhang, X. B. Zhang, *Adv. Funct. Mater.* **2012**, *22*, 3699.
[22] F. Xu, M. Minniti, P. Barone, A. Sindona, A. Bonanno, A. Oliva, *Carbon* **2008**, *46*, 1489.
[23] Z. H. Sheng, L. Shao, J. J. Chen, W. J. Bao, F. B. Wang, X. H. Xia, *ACS Nano* **2011**, *5*, 4350.
[24] G. Wu, N. H. Mack, W. Gao, S. Ma, R. Zhong, J. Han, J. K. Baldwin, P. Zelenay, *ACS Nano* **2012**, *6*, 9764.
[25] E. Yoo, J. Nakamura, H. Zhou, *Energy Environ. Sci.* **2012**, *5*, 6928.
[26] L. Ci, L. Song, C. Jin, D. Jariwala, D. Wu, Y. Li, A. Srivastava, Z. F. Wang, K. Storr, L. Balicas, F. Liu, P. M. Ajayan, *Nat. Mater.* **2010**, *9*, 430.
[27] O. Stephan, P. M. Ajayan, C. Colliex, Ph. Redlich, J. M. Lambert, P. Bernier, P. Lefin, *Science* **1994**, *266*, 1683.
[28] S. M. Yuan, J. X. Li, L. T. Yang, L. W. Su, L. Liu, Z. Zhou, *ACS Appl. Mater. Interfaces* **2011**, *3*, 705.
[29] R. Mi, H. Liu, H. Wang, K. W. Wong, J. Mei, Y. Chen, W. M. Lau, H. Yan, *Carbon* **2014**, *67*, 744.

[30] X. Lin, X. Lu, T. Huang, Z. Liu, A. Yu, *J. Power Sources* **2013**, *242*, 855.
[31] Y. Chen, F. Li, D.-M. Tang, Z. Jian, C. Liu, D. Golberg, A. Yamada, H. Zhou, *J. Mater. Chem. A* **2013**, *1*, 13076.
[32] Y. Li, X. Li, D. Geng, Y. Tang, R. Li, J. P. Dodelet, M. Lefèvre, X. Sun, *Carbon* **2013**, *64*, 170.
[33] Y. Tian, H. Yue, Z. Gong, Y. Yang, *Electrochim. Acta* **2013**, *90*, 186.
[34] K. Guo, Y. Li, J. Yang, Z. Zou, X. Xue, X. Li, H. Yang, *J. Mater. Chem. A* **2014**, *2*, 1509.
[35] Z. Jian, P. Liu, F. Li, P. He, X. Guo, M. Chen, H. Zhou, *Angew. Chem. Int. Ed* **2013**, 53 442.
[36] J. Shui, F. Du, C. Xue, Q. Li, L. Dai, *ACS Nano* **2014**, *8*, 3015.
[37] B. D. McCloskey, D. S. Bethune, R. M. Shelby, T. Mori, R. Scheffler, A. Speidel, M. Sherwood, A. C. Luntz, *J. Phys. Chem. Lett.* **2012**, *3*, 3043.
[38] S. A. Freunberger, Y. Chen, N. E. Drewett, L. J. Hardwick, F. Barde, P. G. Bruce, *Angew. Chem. Int. Ed.* **2011**, *50*, 8609.
[39] R. Younesi, M. Hahlin, F. Björefors, P. Johansson, K. Edström, *Chem. Mater.* **2013**, *25*, 77.
[40] H.-D. Lim, H. Song, H. Gwon, K.-Y. Park, J. Kim, Y. Bae, H. Kim, S.-K. Jung, T. Kim, Y. H. Kim, X. Lepró, R. Ovalle-Robles, R. H. Baughman, K. Kang, *Energy Environ. Sci.* **2013**, *6*, 3570.
[41] R. Black, S. H. Oh, J. H. Lee, T. Yim, B. Adams, L. F. Nazar, *J. Am. Chem. Soc.* **2012**, *134*, 2902.
[42] H. Cheng, K. Scott, *Electrochim. Acta* **2014**, *116*, 51.
[43] Y. C. Lu, Z. Xu, H. A. Gasteiger, S. Chen, K. Hamad-Schifferli, Y. Shao-Horn, *J. Am. Chem. Soc.* **2010**, *132*, 12170.
[44] R. Black, J. H. Lee, B. Adams, C. A. Mims, L. F. Nazar, *Angew. Chem. Int. Ed.* **2013**, *52*, 392.
[45] J. J. Xu, Z. L. Wang, D. Xu, L. L. Zhang, X. B. Zhang, *Nat. Commun.* **2013**, *4*, 2438.
[46] M. M. Ottakam Thotiyl, S. A. Freunberger, Z. Peng, P. G. Bruce, *J. Am. Chem. Soc.* **2013**, *135*, 494.
[47] Z. Zhang, L. Su, M. Yang, M. Hu, J. Bao, J. Wei, Z. Zhou, *Chem. Commun.* **2014**, *50*, 776.
[48] L. Su, Z. Zhou, P. Shen, *J. Phys. Chem. C.* **2012**, *116*, 23974.
[49] M. Yang, Y. Zhong, L. Su, J. Wei, Z. Zhou, *Chem. Eur. J.* **2014**, *20*, 5046.
[50] G. Kresse, J. Hafner, *Phys. Rev. B* **1993**, *47*, 558.
[51] G. Kresse, J. Furthmüller, *Phys. Rev. B* **1996**, *54*, 11169.
[52] J. P. Perdew, J. Chevary, S. Vosko, K. A. Jackson, M. R. Pederson, D. Singh, C. Fiolhais, *Phys. Rev. B* **1992**, *46*, 6671.
[53] P. E. Blöchl, *Phys. Rev. B* **1994**, *50*, 17953.